actuators

MDPI

Article

Development of a 3D-Printed BLDC Motor and Controller for Robotic Applications

Sangsin Park

Department of Mechanical Engineering, Korea National University of Transportation, Chungju-si 27469, Republic of Korea; spark@ut.ac.kr

Abstract

This paper presents the design and experimental validation of a 3D-printed BLDC motor featuring a hollow-shaft rotor and nickel-reinforced stator. The rotor employs neodymium magnets to reduce inertia while maintaining torque density, and the stator integrates thin nickel laminations to improve flux density. A custom controller with Hall sensors, BiSS-C encoder, and CAN interface enables closed-loop position control. Experiments demonstrate stable tracking with short settling time and negligible steady-state error, confirming feasibility for robotic and precision applications.

Keywords: 3D-printed BLDC motor; hollow-shaft rotor; hybrid stator design; BLDC motor controller

1. Introduction

BLDC motors have been extensively adopted in modern electromechanical systems due to their high power density, efficiency, and durability compared to conventional brushed machines [1]. Unlike brushed motors, where mechanical commutation is achieved through brushes and a commutator, BLDC motors rely on electronic commutation governed by rotor position feedback. This design eliminates mechanical wear components, significantly improving reliability and reducing maintenance requirements. Such advantages have made BLDC motors a preferred choice in diverse applications, including robotics, electric vehicles, unmanned aerial systems, precision automation, and biomedical devices [2,3]. In particular, robotic and mechatronic systems impose stringent demands on actuators, requiring lightweight construction, compact integration, high torque-to-weight ratio, and precise position control. Meeting these requirements has driven research into novel BLDC motor designs that not only optimize electromagnetic performance but also incorporate features for sensor integration, compact packaging, and dynamic response.

Traditionally, the fabrication of BLDC motors has relied on subtractive manufacturing methods such as machining, stamping, and lamination. While these methods yield high-performance machines with optimized electromagnetic cores, they are constrained by the geometry achievable through conventional processes. Recent advances in additive manufacturing technologies, such as fused deposition modeling and composite 3D printing, provide opportunities to overcome these constraints by enabling the production of custom, lightweight, and geometrically complex components at relatively low cost and short turnaround times [4,5]. In the context of BLDC motors, additive manufacturing has been used to prototype housings and rotors, demonstrating the feasibility of rapid motor prototyping and design customization. One key advantage of 3D printing is the ability to realize hollow-shaft topologies, which are increasingly important in robotic actuators where

Academic Editors: Dong Jiang, Sizhao Lu and Zewei Shen

Received: 27 August 2025
Revised: 29 September 2025
Accepted: 30 September 2025
Published: 1 October 2025

Citation: Park, S. Development of a 3D-Printed BLDC Motor and Controller for Robotic Applications. *Actuators* **2025**, *14*, 481. https://doi.org/10.3390/act14100481

through-axis cabling, weight reduction, and the integration of secondary components are required. Hollow-shaft configurations reduce the polar moment of inertia, thereby enabling improved transient dynamics such as faster acceleration and deceleration, which are crucial for legged robots, robotic arms, and other precision systems.

An essential aspect of BLDC motor operation is accurate rotor position sensing, which is necessary for electronic commutation and closed-loop control. Hall-effect sensors are widely used for detecting rotor position due to their simplicity, reliability, and low cost. Precise sensor placement relative to the rotor poles is critical to ensuring correct commutation sequences and minimizing torque ripple. Beyond Hall sensors, high-resolution encoders are also required in applications involving precision motion control, such as robotic manipulators and autonomous systems. In addition, the motor controller plays a pivotal role, responsible for commutating motor phases, regulating position, and ensuring robust communication with higher-level control systems. Recent developments in embedded electronics and power conversion circuits have facilitated the integration of compact yet powerful motor controllers, which are indispensable for achieving high-performance robotic actuators.

Akula et al. [6] study the feasibility of fabricating BLDC outrunner rotors using FDM-based 3D printing with PLA composites. Experimental tests comparing 3D-printed and conventional metal rotors show comparable thrust performance, while achieving significant weight reduction. The results highlight the potential of 3D-printed rotors to enhance UAV endurance, reduce costs, and enable customized motor designs.

Shekhar et al. [7] introduced a low-cost modular actuator for robotics, fabricated using additive manufacturing and hobby-grade BLDC motors. The actuator design incorporates 3D-printed planetary gears and custom control electronics, including Arduino and later ESP32 with DRV8305 drivers and AS5147 encoders. Experimental results show competitive torque and performance compared to commercial actuators like GIM8008, at about one-fourth the cost.

Works by Sergio et al. [8] present the design and control of a 3D-printed permanent magnet synchronous motor (PMSM) using PETG material and a Halbach array configuration. A model-based adaptive controller, implemented on Arduino, is developed from system identification to achieve accurate speed reference tracking. Experimental results validate the prototype's performance, showing stable operation, minimal tracking error, and effective thermal behavior under steady-state conditions.

While additive manufacturing has been explored in various electromechanical applications, prior studies have seldom applied 3D-printing techniques directly to the rotor and stator of BLDC motors. Addressing this gap and building on the opportunities it creates, this paper presents the design, fabrication, and experimental validation of a custom 3D-printed BLDC motor with integrated sensing and control, as illustrated in Figure 1. The rotor is designed as a hollow-shaft configuration and equipped with twelve high-energy NdFeB permanent magnets. This configuration not only reduces inertia but also ensures strong magnetic field generation for torque production. The stator incorporates a hybrid design in which hollow stator teeth are reinforced with multiple thin nickel plates, significantly enhancing magnetic flux density while mitigating eddy current losses. Each tooth is wound with enameled copper wire and interconnected into a three-phase Y-configuration, optimized for low-voltage operation and smooth current distribution. Furthermore, a Hall sensor assembly employing three A3144 devices is developed, positioned with precise mechanical spacing to ensure 120° electrical separation of signals for correct commutation. For high-resolution position feedback, a Renishaw BiSS-C absolute encoder with multi-turn capability is integrated, enabling precise angle measurement, even in applications involving gear reduction.

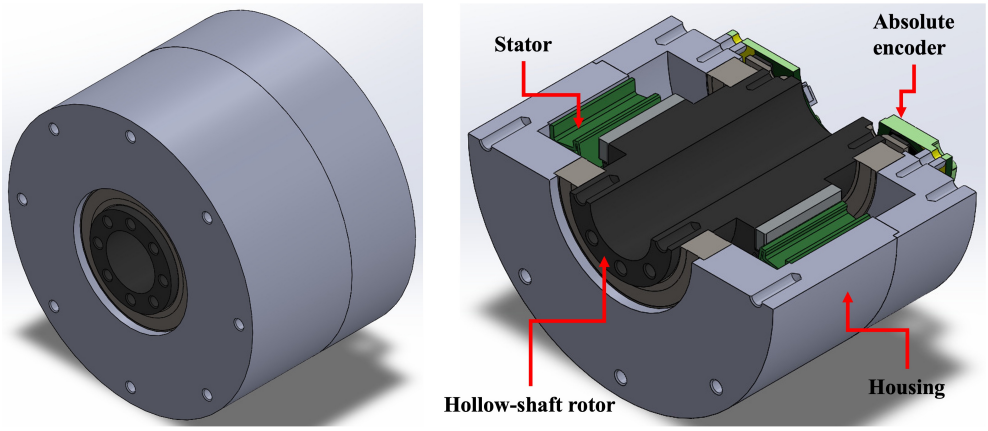

Figure 1. Custom 3D-printed BLDC motor with integrated Hall sensors and BiSS-C absolute encoder for robotic applications.

Complementing the motor design, a custom BLDC motor controller is developed featuring cascaded buck converters for multi-voltage supply, half-bridge MOSFET drivers with current sensing, and RS-422 transceiver-based BiSS-C communication with the encoder. The controller also supports CAN bus communication with a higher-level control system, facilitating integration into robotic platforms. A closed-loop PID position control algorithm is implemented at a 1 kHz update rate to evaluate the system's dynamic performance. The experimental validation of the fabricated motor demonstrates its capability to accurately track commanded step inputs with short settling time and negligible steady-state error. These results confirm that the proposed approach successfully combines additive manufacturing flexibility with enhanced electromagnetic performance and precise sensing to produce a compact and practical actuator solution.

The contributions of this paper are summarized as follows:

1. Development of a hollow-shaft rotor fabricated via additive manufacturing and integrated with NdFeB permanent magnets to reduce inertia and enable through-axis applications;
2. Proposal of a hybrid stator design incorporating 3D-printed structures reinforced with thin nickel laminations to improve magnetic flux density while maintaining manufacturability;
3. Implementation of an integrated sensing system, consisting of Hall-effect sensors and a BiSS-C absolute encoder, to provide both commutation signals and high-resolution angular feedback;
4. Design of a custom BLDC motor controller with cascaded DC–DC converters, half-bridge MOSFET drivers, and CAN communication, enabling reliable closed-loop position control;
5. Experimental validation through step-response testing, demonstrating fast dynamic response, negligible steady-state error, and suitability for robotic actuation.

The paper is organized as follows. Section 2 provides the development of the 3D-printed BLDC motor, including details of the rotor, stator, and Hall sensor. The development of the BLDC motor controller is described in Section 3, and experimental results are presented in Section 4. Finally, discussion and conclusions are described in Sections 5 and 6, respectively.

2. 3D-Printed BLDC Motor

A rotor and a stator of the BLDC motor have been printed in solid fill using a Markforged Mark Two™ 3D printer with a 0.1 mm layer resolution. The printer employs

the Fused Filament Fabrication method with Onyx® composite material, a micro carbon fiber-filled nylon that provides adequate mechanical rigidity.

2.1. Rotor Design

The rotor in the BLDC motor was designed as a hollow-shaft configuration with an inner diameter of 15 mm to accommodate applications requiring through-axis cabling and lightweight structures. The rotor body is illustrated in the 3D CAD model shown in Figure 2. The rotor employed a 12-pole configuration utilizing high-energy neodymium–iron–boron (NdFeB) permanent magnets, each with dimensions of 20 × 10 × 3 mm, positioned on the outer periphery of the rotor, as depicted in Figure 2. Each magnet was bonded to ensure accurate circumferential positioning and uniform air gap distribution. The 12-pole arrangement was selected to achieve a balance between torque density and cogging torque minimization, while maintaining compatibility with the corresponding stator winding configuration [9]. To ensure reliable magnet retention under high rotational speeds, the rotor incorporated dedicated magnet slots with optimized interference fit, supplemented by high-strength adhesive bonding.

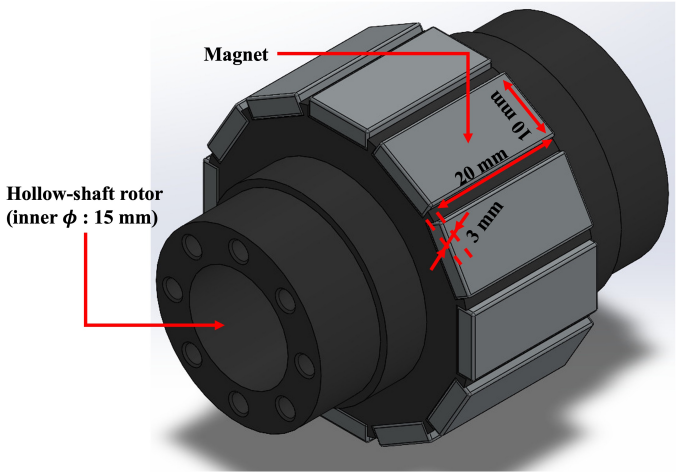

Figure 2. A 3D CAD model of the hollow-shaft rotor (inner diameter: 15 mm) with twelve 20 × 10 × 3 mm NdFeB permanent magnets.

The hollow-shaft topology further contributes to a reduced polar moment of inertia, enabling faster acceleration and deceleration profiles. This feature is particularly advantageous for robotics and precision positioning systems, where dynamic response is critical. The fabricated rotor, shown in Figure 3, demonstrates close agreement with the CAD design in Figure 2, confirming the precision and reproducibility achievable through the selected additive manufacturing approach.

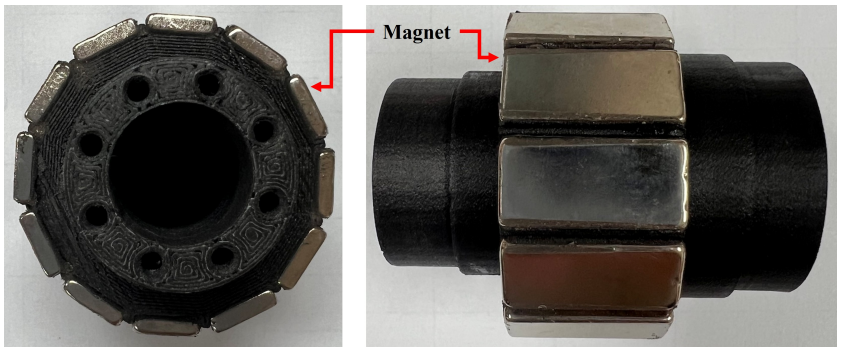

Figure 3. Fabricated hollow-shaft rotor produced via 3D printing and assembled with twelve neodymium permanent magnets.

2.2. Stator Design

The stator was designed with an outer diameter of 60 mm, a thickness of 20 mm, and a total of 18 slots to accommodate the windings. Unlike conventional stator structures, this design incorporated a unique modification to the stator teeth: each tooth contains an internal cavity that allows the insertion of multiple thin nickel plates. These nickel plates, each with a thickness of 0.1 mm, were stacked within the stator teeth, as shown in Figure 4, which illustrates the 3D CAD model in both isometric and top views. The hollow geometry of the teeth is clearly visible in the top view, highlighting the dedicated space for the nickel plate placement.

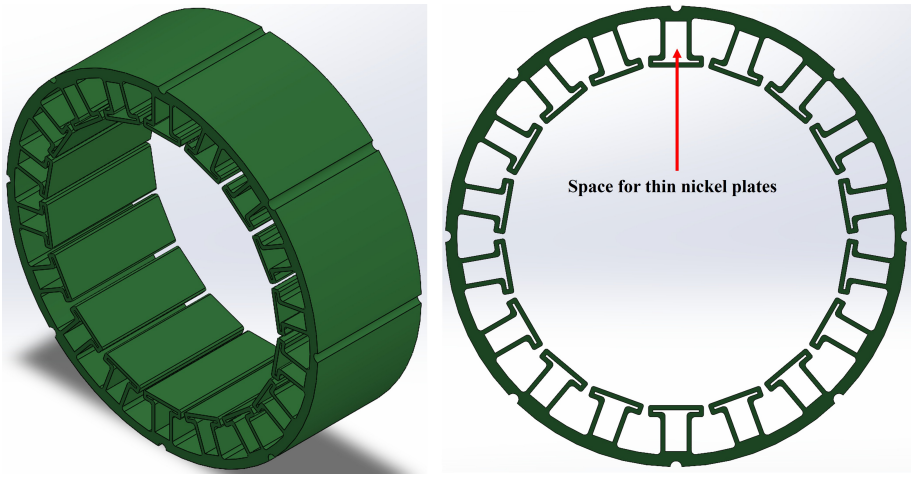

Figure 4. A 3D CAD model of the stator: (**left**) isometric view; (**right**) top view showing the hollow stator teeth designed for thin nickel plate insertion.

The motivation for this design is to enhance the magnetic flux density within the stator by filling the coil region with laminated nickel plates. The thin laminated structure helps to increase the effective magnetic permeability of the tooth while mitigating eddy current losses, thereby improving the overall electromagnetic performance. As shown in Figure 5, multiple nickel plates were inserted into each tooth cavity and, around these reinforced teeth, 0.5 mm diameter enameled copper wire was wound. Each tooth was wound with 16 turns, ensuring a compact winding distribution while maximizing copper fill factor.

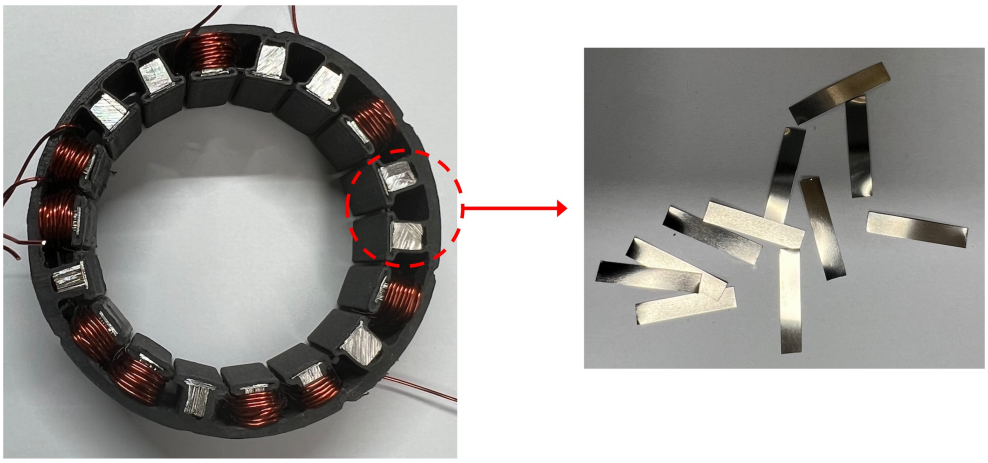

Figure 5. Thin 0.1 mm nickel plates (**right**) and stator teeth reinforced with stacked nickel plates wound with 0.5 mm enameled copper wire (**left**).

The wound coils were then interconnected to form a three-phase configuration, which was terminated in a Y (or star) connection. This configuration was selected due to its

suitability for low-voltage operation and balanced phase currents, enabling smoother motor performance. The completed stator assembly with the Y-connected windings is presented in Figure 6, where the arrangement of the three phases and the final integration of the nickel-reinforced teeth with the windings can be observed. This stator design approach demonstrates a hybrid structure that combines additive manufacturing flexibility with magnetic reinforcement through nickel plate insertion. By doing so, the design not only achieves structural integrity but also improves magnetic field concentration within the stator teeth, potentially increasing torque production and motor efficiency compared to conventional 3D-printed stator geometries.

Figure 6. Completed stator assembly with three-phase windings connected in a Y (or star) configuration.

2.3. Hall Sensor Design

To accurately detect the rotor's angular position, a Hall sensor assembly was designed and implemented. This system utilizes three A3144 Hall-effect switches, which are known for their reliability and precise switching capabilities. The design focused on ensuring signal integrity and optimal sensor placement for the specific motor configuration.

The electrical circuit for the Hall sensor array is depicted in Figure 7. A regulated 5 V DC power source is supplied to each of the three A3144 sensors. To mitigate potential noise on the power supply line, which could cause erratic sensor behavior or false triggering, a bypass capacitor is placed in parallel with each sensor. These capacitors shunt high-frequency noise to the ground, ensuring a stable and clean power input for reliable operation. The circuit outputs three distinct digital signals, designated as Hall_A, Hall_B, and Hall_C, which correspond to the magnetic field detected by each sensor.

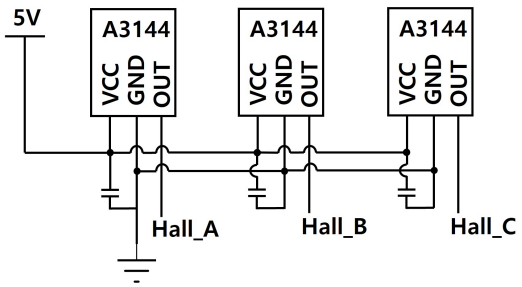

Figure 7. Schematic diagram of the Hall sensor circuit using three A3144 devices, each with a dedicated 5 V supply and bypass capacitor, outputting Hall_A, Hall_B, and Hall_C signals.

The physical placement of the Hall sensors is critical and is determined by the number of magnetic poles on the rotor. The motor in this design features a 12-pole rotor. For proper commutation in a three-phase BLDC motor, the three Hall sensor signals must be

separated by 120 electrical degrees. The relationship between the mechanical angle (θ_m) and the electrical angle (θ_e) is defined by the number of pole pairs (P) on the rotor, as shown in Equation (1):

$$\theta_e = P \cdot \theta_m \tag{1}$$

Given a 12-pole rotor, the number of pole pairs (P) is 6. To achieve the required 120° electrical separation ($\Delta\theta_e$), the necessary mechanical angle separation ($\Delta\theta_m$) between the sensors is calculated as follows:

$$\Delta\theta_m = \frac{\Delta\theta_e}{P} = \frac{120^\circ}{6} = 20^\circ \tag{2}$$

Therefore, the three A3144 Hall sensors are positioned on the PCB with a precise mechanical spacing of 20° relative to each other. This configuration ensures that the output signals (Hall_A, Hall_B, Hall_C) are phase-shifted by 120 electrical degrees, providing the exact rotor position information required by the motor controller. Figure 8 shows the final implementation of the Hall sensor assembly for integration with the motor stator.

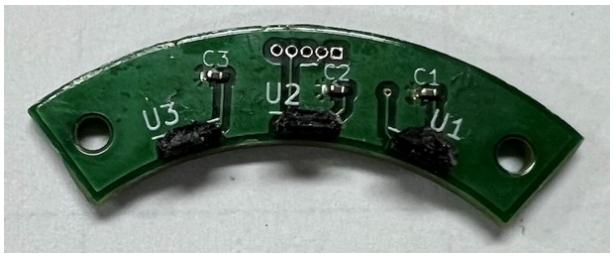

Figure 8. Fabricated Hall sensor PCB with mounted A3144 sensors and bypass capacitors.

2.4. BLDC Motor Assembly

The housing for the BLDC motor was fabricated using a 3D printer with the Onyx®. The BLDC motor has a diameter of 75 mm and a height of 56.3 mm. The assembly process, as illustrated in Figure 9, began with the insertion of the stator into the main housing body. Subsequently, the rotor was positioned in the center of the stator. The assembly was then enclosed with the housing cover, and a Renishaw absolute encoder was installed on the motor. A key feature of the selected encoder is its multi-turn count capability. This allows the encoder to be mounted directly on the motor's input shaft while still enabling the precise measurement of the output shaft's rotation after a reducer is coupled to the motor. This configuration simplifies the design and ensures accurate position tracking through gear reduction. The key specifications of the assembled BLDC motor are summarized in Table 1.

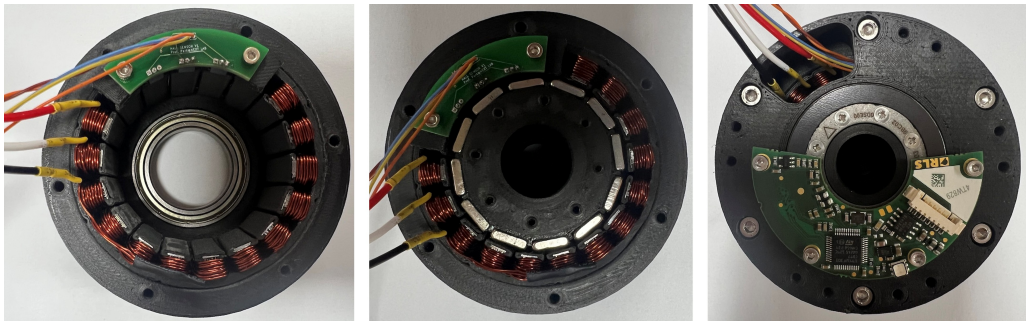

Figure 9. Stepwise assembly process of the 3D-printed BLDC motor: (**left**) stator inserted into the housing body, (**center**) rotor placed at the central axis, and (**right**) completed assembly with absolute encoder.

Table 1. Specifications of the fabricated BLDC motor.

Component	Specification
Total Mass	310 g
Rotor Mass	70 g
Stator Mass	130 g
Other (housing, encoder, etc.)	110 g
Motor Diameter	75 mm
Motor Height	56.3 mm
Number of Poles	12
Number of Slots	18
Encoder Readhead Model #	MB039DCC19MENT00
Encoder Magnetic Ring Model #	MRA039BC020DSE00
Encoder Resolution	19 bit
Encoder Multi-Turn	16 bit
Encoder Interface	BiSS-C

3. BLDC Motor Controller

Figure 10 illustrates the block diagram of the BLDC motor controller. The power supply unit of the controller receives an external 48 V DC input, which is step-down converted sequentially to 12 V, 5 V, and finally 3.3 V through cascaded DC–DC converters. The 12 V output is used to drive the MOSFET driver circuits, the 5 V output supplies power to the Hall sensors and the absolute encoder, and the 3.3 V output is dedicated to powering the MCU.

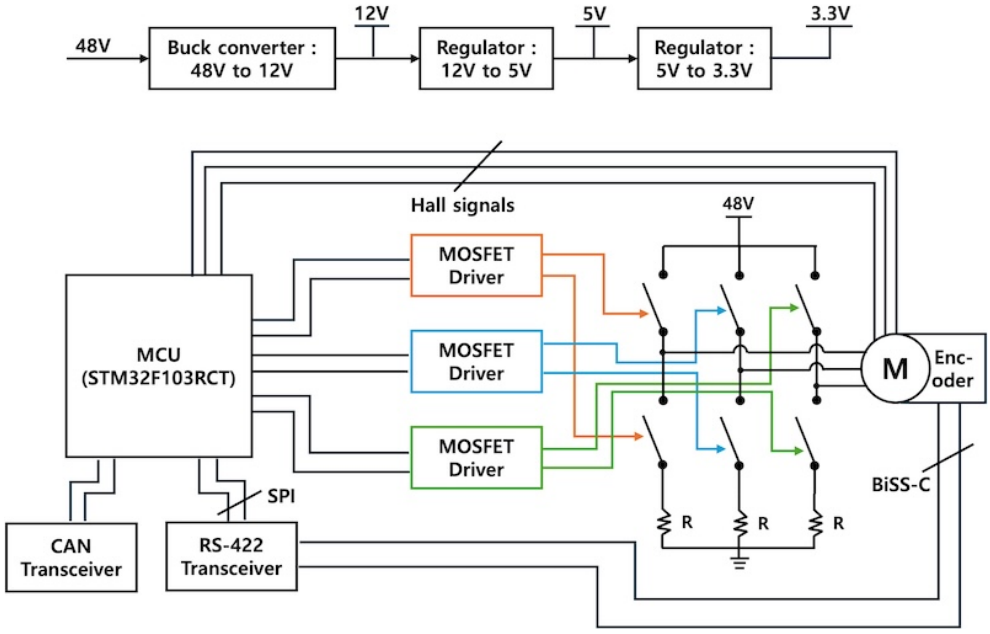

Figure 10. Block diagram of the BLDC motor controller, including the multi-stage DC–DC power supply, three-phase MOSFET H-bridge with driver ICs, BiSS-C absolute encoder interface using RS-422 transceivers, and CAN communication interface with the higher-level controller.

For motor actuation, six N-channel MOSFETs are employed to configure a three-phase H-bridge topology. The switching of the high-side and low-side MOSFETs is controlled by driver ICs. Specifically, three half-bridge MOSFET driver ICs are utilized, each responsible for one phase of the BLDC motor.

The absolute encoder operates with the BiSS-C communication protocol. When the clock signal is provided to the encoder, it responds with the absolute angular position

data. Since the MCU does not natively support BiSS-C communication, SPI is employed to generate the clock and receive the encoder data. Furthermore, because BiSS-C signals are transmitted as differential pairs (clock and data), RS-422 transceiver ICs are used to convert the MCU's single-ended SPI signals into differential signals compatible with the encoder.

For communication with the higher-level controller, a CAN bus interface is adopted. To implement this functionality, the MCU interfaces with an external CAN transceiver IC, enabling reliable high-speed communication in industrial environments.

3.1. Buck Converter Design

For the DC–DC step-down conversion from 48 V to 12 V, a buck converter was designed using the LM5169 controller IC. This device is a synchronous buck regulator optimized for high-voltage applications, and it was selected for its wide input voltage range and robust control scheme. To minimize output ripple and enhance stability, the circuit was configured as shown in Figure 11. The design employs a feedback compensation network consisting of resistors R_{FBT}, R_{FBB} and capacitors C_A, C_B, along with a series resistor R_A. This configuration follows the recommended Type-III compensation scheme [10] to ensure proper loop response while maintaining low output voltage ripple.

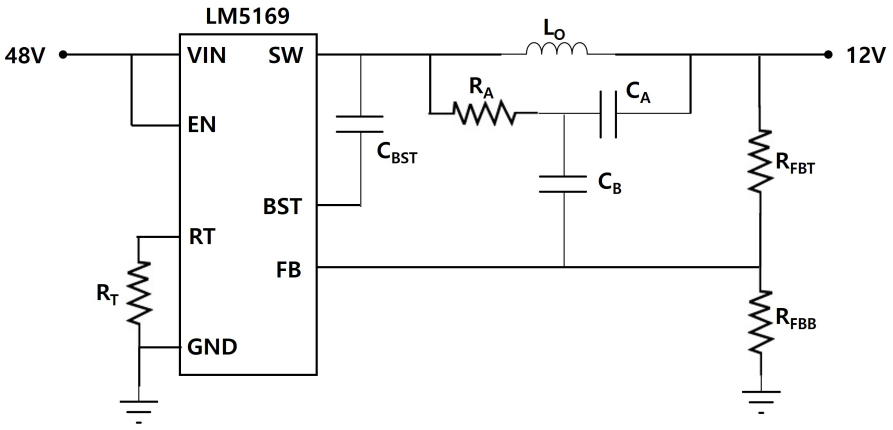

Figure 11. Buck converter design using LM5169, configured for 48 V to 12 V conversion with compensation network for minimum ripple.

3.2. Half-Bridge Driver Design

The circuit for driving each motor phase was based on a half-bridge topology, as illustrated in Figure 12. This design used IPB017N06N3 N-channel MOSFETs for the power switching stage. An IRS2184 gate driver IC was employed to control the high-side and low-side MOSFETs. This driver IC received a PWM signal from the MCU and provided the necessary voltage and current to rapidly switch the MOSFET gates, minimizing switching losses. For phase current measurement, a low-side sensing method was implemented. A 0.005 Ω, 2 W shunt resistor (R_S) was placed between the source of the low-side MOSFET and ground. The voltage drop across this resistor, which was directly proportional to the motor phase current, was detected and amplified by an INA180A1 current sense amplifier. The output signal from the amplifier was then conditioned by a low-pass filter to remove high-frequency noise before being fed into an ADC pin on the MCU for closed-loop control and monitoring.

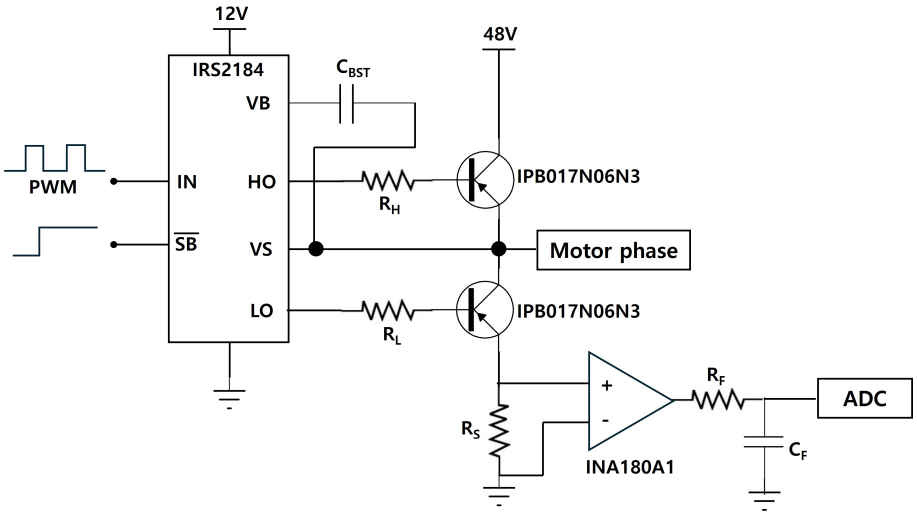

Figure 12. Half-bridge driver design for BLDC motor phase drive using IPB017N06N3 MOSFETs and IRS2184 driver IC. The circuit includes a low-side current sensing resistor (R_S) and INA180A1 current sense amplifier for phase current measurement.

3.3. PCB Prototype Design

The motor controller board was custom-fabricated to align with the motor's hollow-shaft design, resulting in a donut-shaped PCB with a central opening, as shown in Figure 13. The current prototype version was intentionally designed to be larger than the motor itself. This is done to facilitate circuit verification and motor testing by incorporating connectors for the power supply, the three motor phases, and the Hall sensor and encoder signals. This approach follows a two-stage development strategy. The primary objective of this initial, larger version is to thoroughly validate the circuit design and complete comprehensive motor performance tests. Future iterations will focus on miniaturization. The ultimate goal is to develop a fully integrated actuator by mounting a smaller version of this controller board directly onto the rear of the BLDC motor.

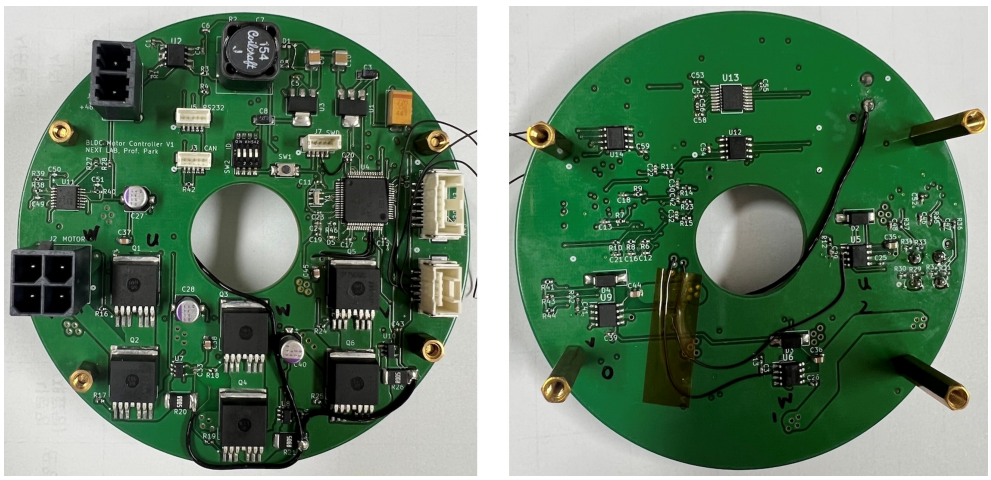

Figure 13. The top (**left**) and bottom (**right**) views of the fabricated motor controller PCB prototype.

A PID control loop for position control, as shown in Figure 14, was implemented on the controller. The PID controller was computed based on the position error, which was the difference between the reference position θ_{ref} and the measured position θ_{meas} from the encoder. θ_{ref} and θ_{meas} are expressed in encoder pulses, and the number of pulses per revolution is 524,288, corresponding to a 19-bit encoder resolution. The PID gains were tuned through a trial-and-error process to achieve a balance between responsiveness and

no overshoot. They are shown in Equation (3), where K_P, K_I, and K_D are the proportional, integral, and derivative gains, respectively. The position control loop operates at a control frequency of 1 kHz.

$$[K_P, K_I, K_D] = [0.2, 0.1, 5.0] \tag{3}$$

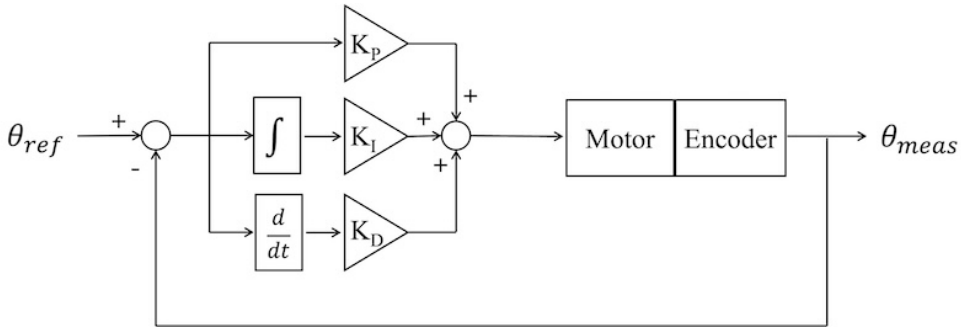

Figure 14. Block diagram of the PID controller for closed−loop position control.

4. Experimental Results

4.1. Step Response Test of the 3D-Printed BLDC Motor

To evaluate the performance of the developed BLDC motor and controller, an experimental setup was configured, as shown in Figure 15. The custom-fabricated BLDC motor was connected to the motor controller board. The controller was then interfaced with a PC via a CAN bus, which allowed for sending commands and receiving real-time data.

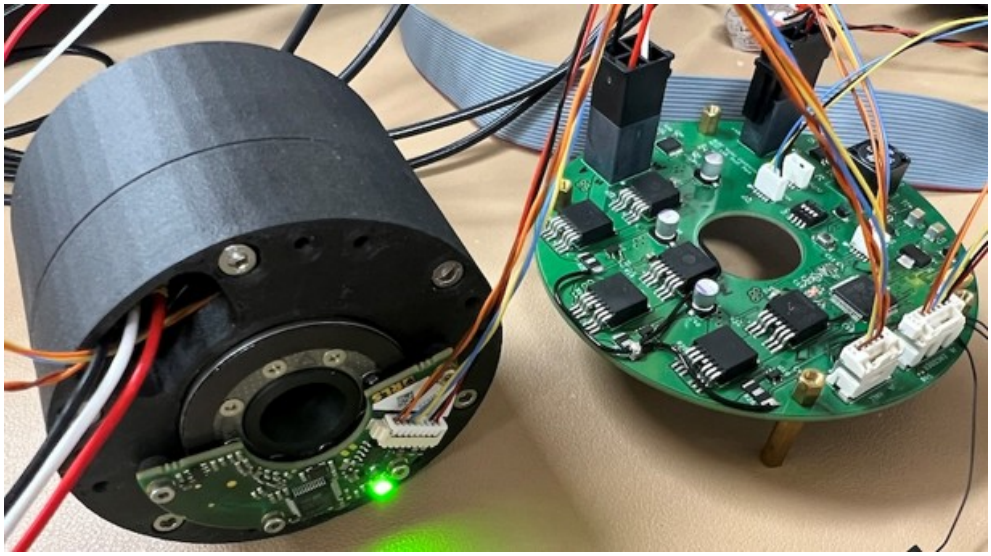

Figure 15. Experimental setup for the motor performance test.

For the initial step input, a target angle of 360° was commanded to the motor. Subsequently, a second step input of 0° was applied to command the motor back to its origin. The experimental results of the step response are illustrated in Figures 16–18. In the plots, the blue dashed line represents the step command (reference) in degrees, while the orange solid line denotes the actual motor response in degrees. Figure 16 shows the motor response to a step command sequence varying between 0° and 360° over a 10-s interval. The motor is clearly observed that the response follows the commanded reference, demonstrating the effectiveness of the implemented controller.

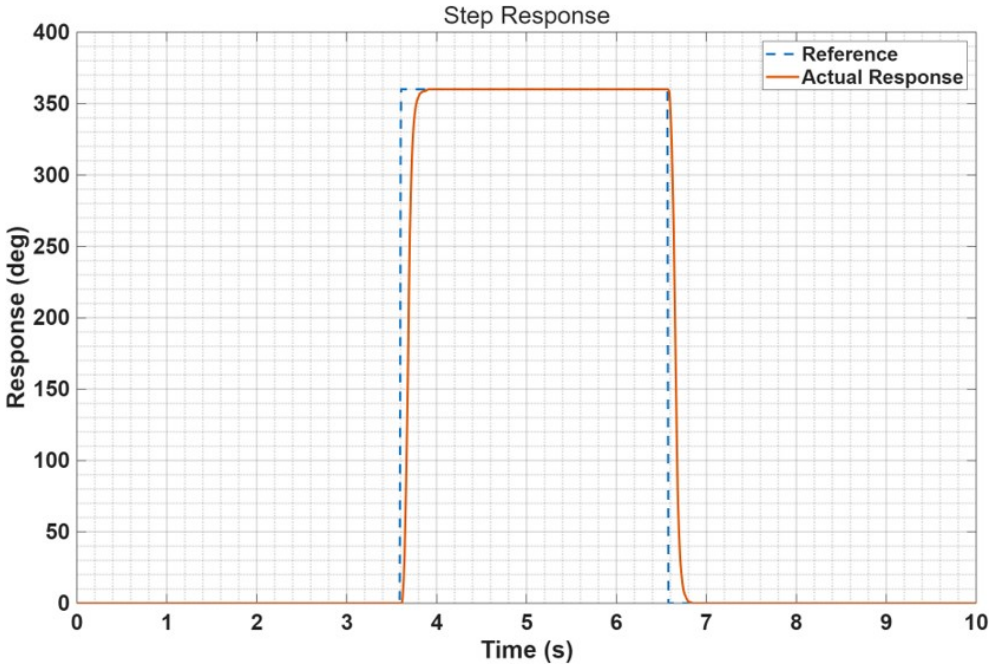

Figure 16. Step response of the BLDC motor to 0°–360°–0° commands over 10 s.

To further examine the transient behavior, Figure 17 presents a magnified view of the time interval from 3.4 s to 4.2 s. At $t = 3.6$ s, the step command reaches 360°, after which the motor response begins to rise. The settling time, defined as the time required for the response to enter and remain within ±2% of the command value (352.8°–367.2°), is measured as 3.78 s. Hence, the motor achieved steady-state operation within 0.18 s after the step input of 360°.

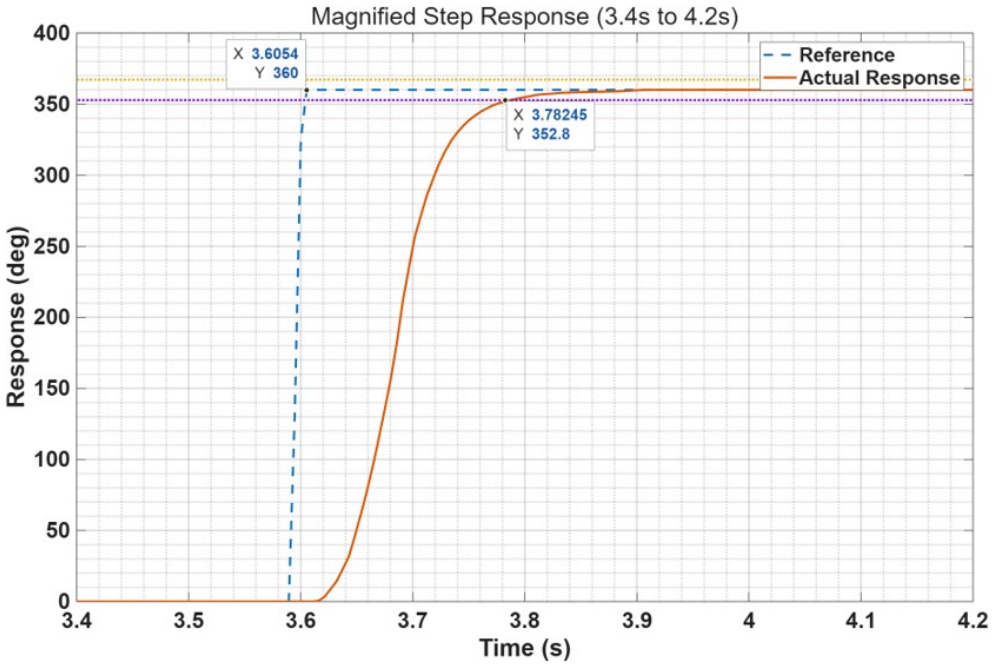

Figure 17. Zoomed view of the motor response between 3.4 s and 4.2 s for the 360° step input. The motor reaches the ±2% settling band at 3.78 s, corresponding to a settling time of 0.18 s.

Figure 18 depicts the error signal of the step response in degrees. At the instant the command is applied ($t = 3.6$ s), the error is 360°. Upon reaching steady state, the residual error is measured as 0.029°, indicating negligible steady-state tracking error.

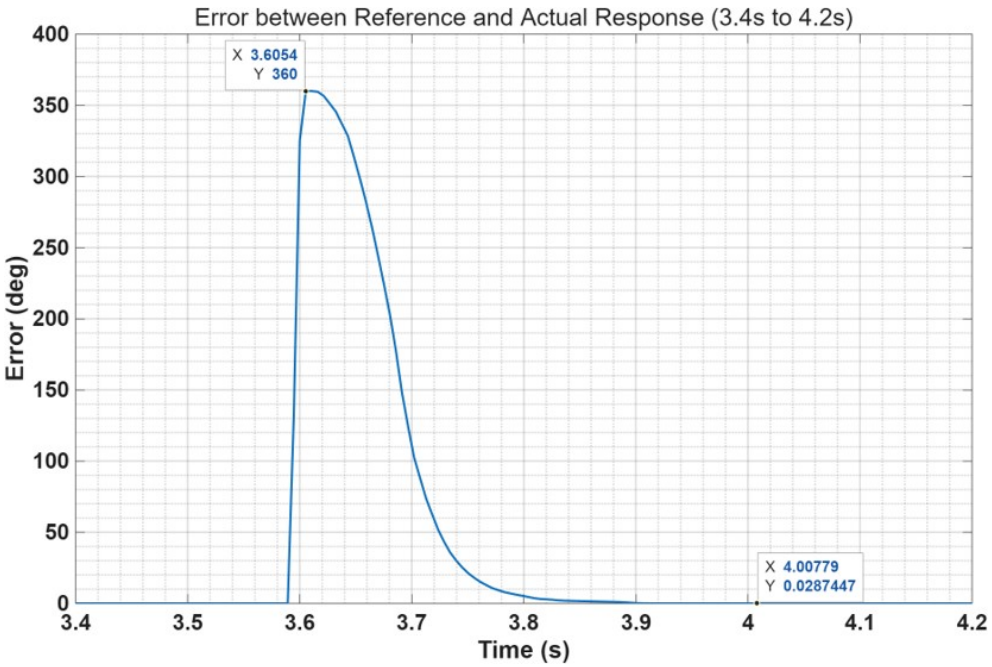

Figure 18. Error response of the BLDC motor to the 360° step command. The error starts at 360° when the step input is applied at 3.6 s and converges to negligible steady-state error.

4.2. Comparision with a Kollmorgen Frameless BLDC Motor

To evaluate the performance of the custom 3D-printed BLDC motor and its controller, a comparative experiment was conducted using an actuator assembled with a Kollmorgen frameless BLDC motor, as shown in Figure 19. The specifications of the frameless BLDC motor are summarized in Table 2. A step input of 30° was applied to the actuator, and the corresponding response is illustrated in Figure 20. Since the actuator is equipped with a planetary gear reducer with a ratio of 11.8335:1, a 30° output displacement corresponds to a motor rotation of 355.005°. The actuator reached the commanded step angle at t = 0.51 s, after which the motor response can be observed. The measured settling time was 0.55773 s, indicating that the motor reached steady state within 0.04773 s. Overall, the actuator exhibited a response approximately 3.77 times faster than that of the custom 3D-printed BLDC motor.

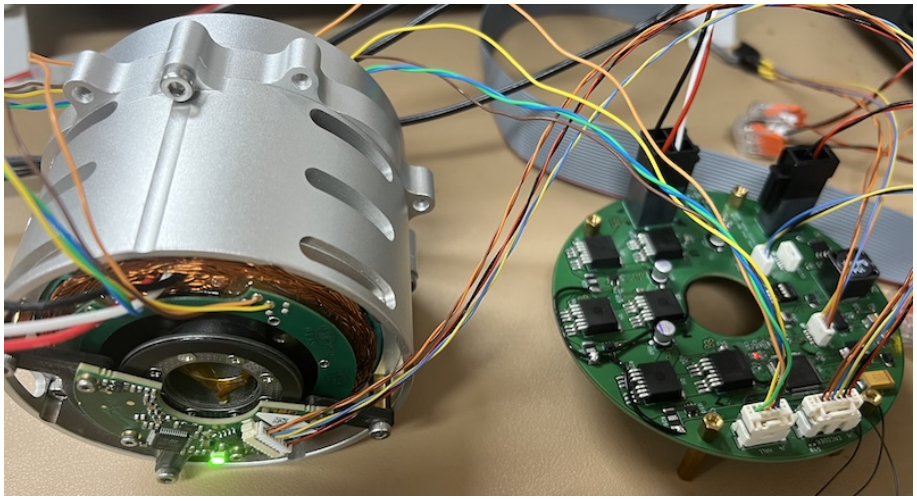

Figure 19. Experimental setup for the Kollmorgen frameless BLDC motor test.

Table 2. Specifications of the Kollmorgen frameless BLDC motor.

Component	Specification
Model Number	TBM-7631-A
Rated Power	307 W
Rated Voltage	48 V
Rated Torque	1.65 Nm
Rated Current	10.9 A
Total Mass	0.738 kg

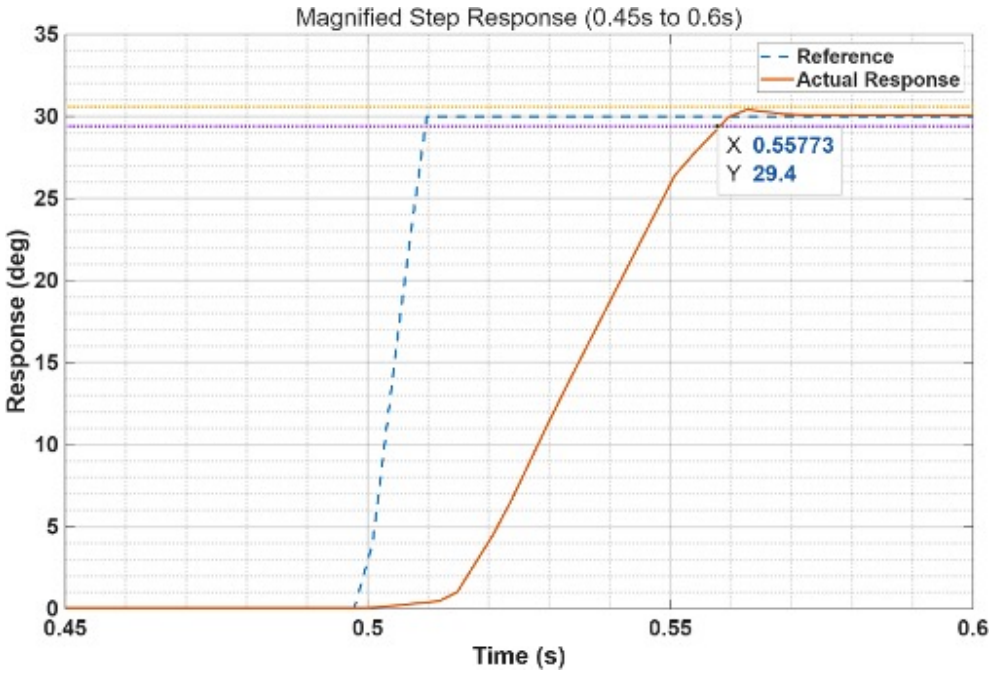

Figure 20. Magnified step response of the Kollmorgen motor between 0.46 s and 0.6 s for the 30° step input. Its settling time is 0.04773 s.

Although its performance is lower than that of commercial high-power, high-torque motors, the proposed BLDC motor can be fabricated at a cost of approximately 44 USD (see Table 3), and further performance improvements are expected through design refinements of the stator and rotor structures. Moreover, the developed BLDC motor controller is readily applicable to commercial high-power motors.

Table 3. Estimated development cost of the 3D-printed BLDC motor and controller.

Component	Cost (USD)
Rotor (3D printing)	7.43
Stator (3D printing)	3.06
Housing body (3D printing)	11.67
Housing cover (3D printing)	7.16
Bearings	4.5
Magnets	7.1
Coil and nickel plates	3.0
Hall sensor PCB (prototype)	20.69
Controller PCB (prototype)	45.67
Controller components	45.0
Absolute encoder	305.14
Total	460.42

5. Discussion

Through a trial-and-error process, the rotor and stator designs were progressively improved. Figure 21 illustrates the early design of the rotor. In this configuration, the absence of partitions between adjacent magnets caused them to adhere to one another during assembly, necessitating the use of a dedicated magnet alignment jig. In contrast, the current rotor design shown in Figure 3 incorporates partitions between magnets, thereby eliminating the need for such a jig during magnet placement. Figure 22 presents the early designs of the stator. The left shows an outer-rotor-type stator specifically designed to facilitate manual coil winding. The right depicts the first nickel-reinforced stator. However, in this early design, the thin nickel plates attached to the inner surfaces of the stator teeth frequently detached, representing a major drawback of the configuration.

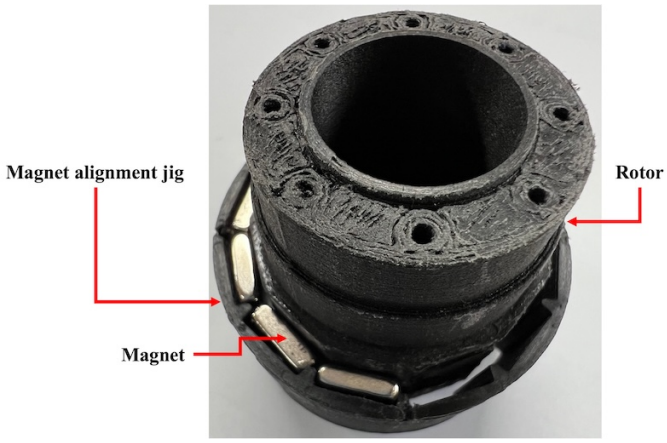

Figure 21. Early design of the rotor, showing the need for a magnet alignment jig to ensure precise magnet placement.

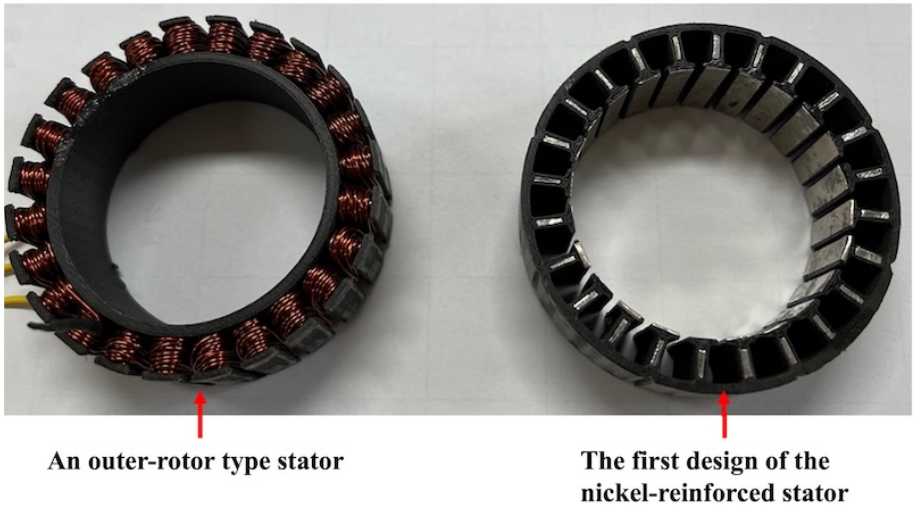

Figure 22. Early designs of the stator: (**left**) an outer-rotor-type stator designed to facilitate manual coil winding easily, (**right**) the first nickel-reinforced stator.

During the continuous operation of the fabricated BLDC motor, a noticeable increase in the housing temperature is observed. The observed temperature of the housing is 64.3 °C after about 30 min of continuous operation. However, the material used for 3D printing, Onyx®, has a maximum operating temperature of 145 °C [11]. Unlike conventional motors, which are typically made of metal and thus benefit from favorable thermal conductivity, the 3D-printed BLDC motor relies on non-metallic components, making it less efficient in dissipating heat. To address this limitation, design modifications such as incorporating

ventilation holes into the motor housing will be implemented in the next fabrication cycle. Furthermore, the motor will be coupled with a reduction gearbox to conduct realistic load tests. In this context, robust PID control strategies applicable to nonlinear systems will be considered, with related approaches discussed by Skrjanc et al. [12] and Wen et al. [13]. Finally, to consider BLDC motors without Hall sensors, additional circuitry will be integrated into the controller to enable sensorless control, with reference to the approach discussed by Xu et al. [14], and the firmware will be updated accordingly.

6. Conclusions

In this work, a 3D-printed BLDC motor with a hollow-shaft rotor and a nickel-reinforced stator was developed together with an integrated sensing and control system. The hybrid approach combined the design flexibility of additive manufacturing with improved electromagnetic performance through thin nickel laminations, while the custom controller enabled reliable operation with Hall sensors, an absolute encoder, and CAN communication. Experimental validation confirmed the effectiveness of the proposed design. The motor exhibited stable step responses, with a short settling time of 0.18 s and negligible steady-state error, demonstrating that the system can accurately track position commands under closed-loop control. These results verify that the presented actuator design can meet the performance requirements of robotics and precision motion applications.

Future work will focus on the further miniaturization of the motor controller, the optimization of winding and cooling strategies, and extended testing under practical load conditions. By advancing toward fully integrated actuator modules, the proposed design has the potential to contribute to the development of next-generation robotic systems requiring lightweight, customizable, and high-performance BLDC motors.

Funding: This research received no external funding.

Institutional Review Board Statement: Not applicable.

Informed Consent Statement: Not applicable.

Data Availability Statement: The original contributions presented in this study are included in the article. Further inquiries can be directed to the corresponding author.

Acknowledgments: This work was supported by Korea National University of Transportation in 2025.

Conflicts of Interest: The author declare no conflicts of interest.

Abbreviations

The following abbreviations are used in this manuscript:

FDM	Fused Deposition Modeling
PLA	Polylactic Acid
CAD	Computer-Aided Design
BLDC	Brushless Direct Current
PCB	Printed Circuit Board
PID	Proportional-Integral-Derivative
MCU	Microcontroller Unit
PWM	Pulse Width Modulation
ADC	Analog-to-Digital Converter
SPI	Serial Peripheral Interface
MOSFET	Metal-Oxide-Semiconductor Field-Effect Transistor
CAN	Controller Area Network

References

1. Kim, H.; Lee, Y.; Ko, S.; Jo, N.; Kim, W. Design Process of High-Power Density Hybrid Type Motor Using 3D Printing. *IEEE Access* **2025**, *13*, 32072–32086. [CrossRef]
2. Mohanraj, D.; Aruldavid, R.; Verma, R.; Sathiyasekar, K.; Barnawi, A.; Chokkalingam, B.; Mihet-Popa, L. A Review of BLDC Motor: State of Art, Advanced Control Techniques, and Applications. *IEEE Access* **2022**, *10*, 54833–54869. [CrossRef]
3. Kim, J.; Kang, T.; Song, D.; Yi, S. Design and control of a open-source, low cost, 3d printed dynamic quadruped robot. *Appl. Sci.* **2021**, *11*, 3762. [CrossRef]
4. Bridges, S.; Smith, G.; Preston, R.; Sevil, H.E.; Reynolds, M. BLDC Actuators Revisited: A New Cost-Effective Design and Manufacturing for Robotic Applications. In Proceedings of the 35th Florida Conference on Recent Advances in Robotics, Tampa, FL, USA, 18–20 May 2023.
5. Mettes, S.; Schwalbe, J.; Allen, K.; Mazumdar, Y. Fully 3D-Printed Multilayer Axial Flux Stator for Rotary Electromagnetic Motors. *IEEE/ASME Trans. Mechatron.* **2024**, *29*, 2903–2910. [CrossRef]
6. Akula, V.; Goyal, K.; Verma, O.; Gupta, V. Feasibility study of a 3D printed BLDC outrunner rotor. *Mater. Today Proc.* **2023**, *80*, 163–167. [CrossRef]
7. Shekhar, S.; Tiwari, U.; Gandhi, M.; Tripathi, S. Low Cost Modular Actuator Fabrication with Aid of Additive Manufacturing, Utilizing Brushless D.C. Motor and Its Control Electronics for Robotics Application. *J. Mob. Multimed.* **2025**, *21*, 693–712. [CrossRef]
8. Sergio, V.; Alexander, M.; Eduardo, G. Model-Based Adaptive Control of a 3D Printed Permanent Magnet Synchronous Motor. *Eng. Lett.* **2023**, *31*, 1804–1812.
9. Hanselman, D. *Brushless Permanent Magnet Motor Design*, 3rd ed.; Magna Physics Publishing: Lebanon, OH, USA, 2006; pp. 229–294.
10. Texas Instruments. LM516x, 0.65 A/0.3 A, 120 V Absolute Maximum, Step-Down Converter with Fly-Buck™ Converter Capability. Available online: https://www.ti.com/product/LM5169 (accessed on 27 August 2025).
11. Markforged. Material Datasheet: Composites. Available online: https://markforged.com/materials/plastics/onyx (accessed on 29 September 2025).
12. Skrjanc, I.; Blazic, S.; Angelov, P. Robust evolving cloud-based PID control adjusted by gradient learning method. In Proceedings of the 2014 IEEE Conference on Evolving and Adaptive Intelligent Systems (EAIS), Linz, Austria, 2–4 June 2014; pp. 1–8.
13. Wen, J.; Wang, F. Stable Levitation of Single-point Levitation Systems for Maglev Trains by Improved Cascade Control. *Rom. J. Inf. Sci. Technol.* **2024**, *27*, 348–361. [CrossRef]
14. Xu, R.; Shen, X.; Lin, X.; Liu, Z.; Xu, D.; Liu, J. Robust Model Predictive Control of Position Sensorless-Driven IPMSM Based on Cascaded EKF-LESO. *IEEE Trans. Transp. Electrif.* **2025**, *11*, 8824–8832. [CrossRef]